Estimating Vignetting Function from a Single Image for Image Authentication

Siwei Lyu
Computer Science Department
University at Albany, SUNY
Albany, NY 12222
lsw@cs.albany.edu

ABSTRACT

Vignetting is the phenomenon of reduced brightness in an image at the peripheral region compared to the central region. As patterns of vignetting are characteristics of lens models, they can be used to authenticate digital images for forensic analysis. In this paper, we describe a new method for model based single image vignetting estimation and correction. We use the statistical properties of natural images in the discrete derivative domains and formulate the vignetting estimation problem as a maximum likelihood estimation. We further provide a simple and efficient procedure for better initialization of the numerical optimization. Empirical evaluations of the proposed method using synthesized and real vignetted images show significant gain in both performance and running efficiency in correcting vignetting from digital images, and the estimated vignetting functions are shown to be effective in classifying different lens models.

Categories and Subject Descriptors

I.4 [**Image Processing**]: Miscellaneous

General Terms

Algorithms

Keywords

vignetting function estimation, camera identification

1. INTRODUCTION

When taking a photograph using a camera, the volume of light transmitted to the image sensor tends to decrease from the center of the image to the corners, a phenomenon commonly known as *vignetting* [26]. The reduction of light due to vignetting is at its worst when lenses are focused at infinity with a large field of view. Because vignetting is the result of the physics of light and geometric shape of the lenses, it cannot be completely eliminated. Indeed, small amount of vignetting is usually purposefully incorporated in the lens design to improve other attributes such as contrast and sharpness. Artificial vignetting effects are also intentionally added to an image, by burning the outer edges of the photograph for film stock or using digital imaging techniques such as the *Lens Correction* filter in Photoshop, to draw attention to the central subject in the image. As different lenses have slightly different vignetting patterns, it is possible to identify lenses using the specific way they cause vignetting. Such can provide useful information in deciding the authenticity of an image for forensic analysis [7]. On the other hand, with an estimated vignetting pattern, we can remove vignetting effects from images where the attenuation of brightness is undesirable, or accurate intensity values are needed.

In this work, we describe a new method to estimate vignetting function, which approximates the light attenuation pattern of a lens, from a single vignetted image. Our basic methodology is that, based on a parametric vignetting function, we aim to factorize the intensities of a vignetted image into the product the intensities of the original image and the vignetting function. When using only one observed vignetted image, this is an ill-posed problem, as many different combinations of image intensities and vignetting functions can produce the same observed vignetted image. To obtain a feasible solution, following a general methodology widely adopted recently in solving many ill-posed low level computer vision problems [20, 1, 27, 9], we take advantage of some regular statistical properties of natural photographic images with no vignetting effects in the derivative domain, and formulate the estimation of the vignetting function as maximum likelihood optimization. Further, as the initial values of parameters are critical for the performance and efficiency of the nonlinear optimization, we develop a simpler and more efficient vignetting estimation method based on a Gaussian approximation to the parametric vignetting model, whose results are used to initialize the nonlinear optimization procedure.

In comparison with several recent works of single image vignetting correction [34, 35], the method we propose has two important advantages. First, unlike previous methods, our method does not require the vignetting function to be centered at the image center – it estimates the vignetting center from the vignetted image as part of the procedure. Because of this, our method can be applied when the vignetted image is cropped off-center. Further, previous works typically assume circular shaped vignetting functions. However, it is known that for wide-angle lenses with large aperture, the vignetting contour is not circular but elliptical [19]. In contrast, our method is able to estimate elliptical shaped vignetting functions. Using the estimated vignetting function from a vignetted image, we study the effectiveness of vignetting patterns in identifying lens models for digital forensics. We also demonstrate the performance of the estimated vignetting function in correcting the intensities of a vignetted image.

MM&Sec'10, September 9–10, 2010, Roma, Italy.

2. RELATED WORK

Vignetting is usually modeled as the multiplication of the image intensities with a spatially varying vignetting function. Correcting the vignetting effect is easy if the vignetting function is known or can be calculated from lens parameters. For high-end digital cameras, such lens parameters can be stored in the digital processors for known lens types, and used to correct vignetting at the time when an image is captured, an example of such function is the *Peripheral Illumination Correction* in the recent Cannon EOS series cameras. Another simple approach to obtain lens vignetting pattern is by calibration using an image of uniform brightness [29, 2, 17, 33]. On the other hand, if the camera is not at one's disposal, the vignetting function can be estimated using a sequence of images of a static scene captured with the same camera/lens combination [11, 15, 21].

Perhaps the most challenging case of estimating vignetting function is when we only have a single vignetted image and no specific information about the source camera/lens. The first method for single image vignetting correction was [34], where the vignetted image is segmented into texture and non-texture regions, and the vignetting function is estimated from the non-texture regions with distinct structures using a robust outlier exclusion procedure. However, the segmentation step in this method is relatively slow, and can introduce errors that significantly affect the final vignetting correction. An improved method was described in [35] based on the empirically observed symmetry in the distributions of radial derivatives, which are differential operations along the radial axis originating from the image center. As no segmentation is required, this method achieves improvement in both performance and running time. However, in practice, the estimation of radial derivatives is numerically instable, which can lead to a large bias to the estimated vignetting function. More important, both methods are limited in two aspects. First, both assume that the center of the vignetting function is known and coincides with the geometric center of the vignetted image. Second, both rely on the assumption that the shape of the vignetting function is circular. These limitations constrain the applicability of these methods to the more general situations such as the vignetted image has been cropped off-center, or the vignetting pattern involved does not have a circular shape.

Using general camera/lens characteristics for the authentication of digital images in forensic analysis has recently received a lot of attention, notable examples include image sensor noise [6], interpolation patterns in color filter arrays [25], lens chromatic aberrations [16], intrinsic fingerprints [18, 31], and camera response functions [12], and an extensive evaluation for some general image features for camera model identification in [10]. Since vignetting pattern is a specific characteristic for different camera/lens, it is possible to employ an estimated vignetting function as a basis for camera/lens identification and image authentication. To our best knowledge, however, there has not been any previous systematic study of such an approach.

3. VIGNETTING ESTIMATION

In this section, we describe in detail our method to estimate vignetting function from a single image. To simplify the subsequent discussion, let us assume that the origin of the coordinate system for $\mathbf{v} = (x, y)^T$ is at the geometric center of the image. According to the general observation of vignetting effect [26], the intensity at a pixel location $\mathbf{v} = (x, y)^T$ in a vignetted image, $I_v(x, y)$, can be closely approximated as the product of the intensity of the original image, $I(x, y)$, and a parametric vignetting function $\phi(\mathbf{v}; \theta)$, as:

$$I_v(\mathbf{v}) = I(\mathbf{v})\phi(\mathbf{v}; \theta), \tag{1}$$

where we use θ to represent all parameters of the vignetting function. In this work, we adopt a generalization of the Kang-Weiss vignetting model [17] for $\phi(\mathbf{v}; \theta)$, which allows for a center differing from the geometric center of the original image, and elliptical contours for the vignetting function. Specifically, the vignetting function model we use is

$$\phi(\mathbf{v}; \theta) = A(\mathbf{v}; \mathbf{c}, P)G(\mathbf{v}; \{\alpha_i\}_{i=1}^k). \tag{2}$$

$A(\mathbf{v}; \mathbf{c}, P)$ is the illumination factor and is defined as

$$A(\mathbf{v}; \mathbf{c}, P) = \frac{1}{\left(1 + \left(\frac{r}{2}\right)^2\right)^2},$$

where

$$\mathbf{c} = \begin{pmatrix} c_1 \\ c_2 \end{pmatrix}, P = \begin{pmatrix} p_1 & p_2 \\ p_2 & p_3 \end{pmatrix},$$

are the center and the shape matrix of the vignetting function, respectively, and

$$r = \sqrt{(\mathbf{v} - \mathbf{c})^T P (\mathbf{v} - \mathbf{c})},$$

is the Mahalanobis distance of $\mathbf{v}$ to the center $\mathbf{c}$. Unlike the original Kang-Weiss model, in our generalization, the effective focal length f of the vignetting function is implicit in the shape matrix P: for a circular vignetting function, one has $p_1 = p_3 = 1/f^2$ and $p_2 = 0$. $G(\mathbf{v}; \{\alpha_i\}_{i=1}^k)$ is the geometric factor of the vignetting function and we use a polynomial of r as in [35]:

$$G(\mathbf{v}; \{\alpha_i\}_{i=1}^k) = 1 - \sum_{i=1}^{k} \alpha_i r^i.$$

We fix the degree of the polynomial to $k = 7$. For conciseness, we will use $A(\mathbf{v})$ and $G(\mathbf{v})$ instead to denote these functions subsequently. Correspondingly, our goal in this work is to obtain parameters in the vignetting function, θ, and recover the intensities of the original image $I(\mathbf{v})$, using a single observed vignetted image I_v. It is more advantageous to take logarithm on both sides of Eq.(1) to obtain a linear equation, as:

$$i_v(\mathbf{v}) = i(\mathbf{v}) + \log A(\mathbf{v}) + \log G(\mathbf{v}), \tag{3}$$

where $i(\mathbf{v})$ and $i_v(\mathbf{v})$ denote $\log I(\mathbf{v})$ and $\log I_v(\mathbf{v})$, respectively. Then, with an input $i_v(\mathbf{v})$, we aim to split it into the sum of three terms $i(\mathbf{v})$, $\log A(\mathbf{v})$ and $\log G(\mathbf{v})$. As can be easily seen, there exist many different combinations of $i(\mathbf{v})$, $\log A(\mathbf{v})$ and $\log G(\mathbf{v})$ whose sum is $i_v(\mathbf{v})$, and thus the problem is intrinsically ill-posed. However, this can be alleviated by searching $i(\mathbf{v})$ that are consistent with those of natural photographic images without significant vignetting effects. Such consistency is evaluated in the discrete derivative domains as described in the following.

3.1 Discrete Derivative Operators

We use D_Δ^r to denote discrete derivative operators used in this work, where superscript $t \in \{x, y, xx, xy, yy\}$ corresponds to the type of derivatives (e.g., D_Δ^x is the first order horizontal derivative), and Δ is the step size in computing such derivatives. Specifically, these operators are defined, as:

$$\begin{aligned}
D_\Delta^x I(x,y) &= I(x+\Delta, y) - I(x,y), \\
D_\Delta^y I(x,y) &= I(x, y+\Delta) - I(x,y), \\
D_\Delta^{xx} I(x,y) &= I(x+\Delta, y) + I(x-\Delta, y) - 2I(x,y), \\
D_\Delta^{yy} I(x,y) &= I(x, y+\Delta) + I(x, y-\Delta) - 2I(x,y), \\
D_\Delta^{xy} I(x,y) &= I(x+\Delta, y+\Delta) - I(x, y+\Delta) \\
&- I(x+\Delta, y) - I(x,y).
\end{aligned}$$

Note that when applied to an image, these discrete derivative operators can be efficiently implemented as convolution of the image with appropriate filters[1]. Conceptually, the discrete differential operators, after normalizing with the step size, implement the corresponding continuous differential operators on the discrete pixel lattice. For instance $\frac{1}{\Delta}D^x_\Delta$ corresponds to $\frac{\partial}{\partial x}$, and $\frac{1}{\Delta^2}D^{xx}_\Delta$ corresponds to $\frac{\partial^2}{\partial x^2}$.

We then apply the five discrete derivative operators to both sides of Eq.(3), which yields

$$D^r_\Delta i_v(\mathbf{v}) = D^r_\Delta i(\mathbf{v}) + D^r_\Delta \log A(\mathbf{v}) + D^r_\Delta \log G(\mathbf{v}). \quad (4)$$

Note that Eq.(4) holds for each pixel location $\mathbf{v}$. The spatially varying $\log A(\mathbf{v})$ and $\log G(\mathbf{v})$ make the relation between $D^r_\Delta i_v(\mathbf{v})$ and $D^r_\Delta i(\mathbf{v})$ inhomogeneous, the farther $\mathbf{v}$ is away from the vignetting center $\mathbf{c}$, the larger the shift given by $D^r_\Delta \log A(\mathbf{v}) + D^r_\Delta \log G(\mathbf{v})$. This spatial inhomogeneity makes direct estimation of the parameters difficult, and is solved by taking average both sides of Eq.(4) over all pixel locations $\mathbf{v}$. Specifically, this leads to a new relation that holds for each individual vignetted image I_v, as:

$$\overline{D^r_\Delta i(\mathbf{v})} = \overline{D^r_\Delta i_v(\mathbf{v})} - \overline{D^r_\Delta \log A(\mathbf{v})} - \overline{D^r_\Delta \log G(\mathbf{v})}, \quad (5)$$

where the bars denote the averaging operation over all $\mathbf{v}$ in the image plane. Eq.(5) shows that in the discrete derivative domains, the spatially averaged response of the original image, $\overline{D^r_\Delta i_v(\mathbf{v})}$, can be obtained from that of the observed vignetted image $\overline{D^r_\Delta i(\mathbf{v})}$, by adjusting with a value, $\overline{D^r_\Delta \log A(\mathbf{v})} + \overline{D^r_\Delta \log G(\mathbf{v})}$, that is completely determined by the vignetting function. Term $\overline{D^r_\Delta i(\mathbf{v})}$ is not directly accessible as it reflects properties of the original image without vignetting. But we can seek vignetting function parameters θ that make $\overline{D^r_\Delta i_v(\mathbf{v})} - \overline{D^r_\Delta \log A(\mathbf{v})} - \overline{D^r_\Delta \log G(\mathbf{v})}$ consistent with $\overline{D^r_\Delta i(\mathbf{v})}$ for natural images. The essential component for this method is then the common and regular statistical properties of $\overline{D^r_\Delta i(\mathbf{v})}$, which are discussed in the following.

3.2 Natural Image Statistics in the Derivative Domains

Images resembling scenes from the physical world are loosely tagged as *natural images*, and are known to occupy only a small fraction of all possible images [28]. More importantly, natural images have regular statistical properties that distinguish them from random images [14]. Over the past two decades, many regular statistical properties of natural images have been observed. One particular stable observation is that natural images tend to have heavy tailed non-Gaussian marginal distributions in the general band-pass domains [4]. Furthermore, these marginal densities can be well fit with the generalized Laplacian density (sometimes also known as the generalized Gaussian density) [23, 30, 13], defined as

$$p(x) = \frac{p}{2\gamma\Gamma(1/\beta)} \exp\left(-|x/\gamma|^\beta\right),$$

with γ and β being the model parameters and $\Gamma(\cdot)$ being the standard Gamma function. The non-Gaussian characteristics and close approximation with the generalized Laplacians of the marginals are robust to point-wise nonlinear transforms of pixel intensities such as the logarithm [28] and specific choices of the band-pass domains, of which the derivative domains used in this paper are special cases [3].

However, to tackle the vignetting estimation problem in Eq.(5), we need to investigate the statistical properties of the *spatial averages* of the derivative domain responses of natural images, $\overline{D^t_\Delta i(\mathbf{v})}$, instead of the responses ($D^t_\Delta i(\mathbf{v})$) themselves. To our knowledge, there has no previous systematic study of this aspect of natural image statistics. For an empirical evaluation, we collect $20,000$ randomly chosen pixel blocks of size 200×200 from images in the Van Hateren image database [32]. These grayscale images are obtained from calibrated cameras with no obvious vignetting effects and linearized intensities. We first log transform the pixel intensity, then apply the discrete derivative operators to the log pixel intensities of each image block. We then collect the mean discrete derivative domain response for each of the $20,000$ blocks and obtain their histograms. These histograms are shown in the log domain in Fig.1 (green solid curves) for different $\overline{D^t_\Delta i(\mathbf{v})}$ and Δ values (columns). For the sake of comparison, Gaussian densities with the same means and variances are shown as red dashed curves. Also shown as black dashed curves in each plot are the optimal fitting (using the method of moment matching [30]) of the generalized Laplacian density to these histograms.

From this experiment, we note that the histograms of the mean responses of natural images in the discrete derivative domain, similar to those of the raw derivative domain responses, have means close to zero and show strong non-Gaussian characteristics. Furthermore, they can also be well approximated with generalized

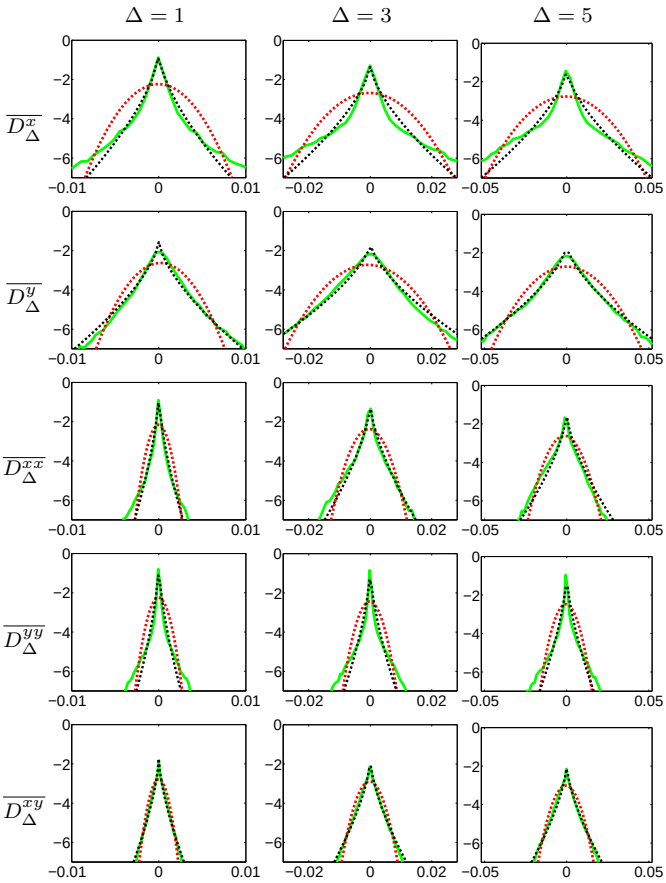

Figure 1: Log marginal histograms (green solid curves) for different $\overline{D^t_\Delta i(\mathbf{v})}$ and Δ obtained with randomly chosen blocks from the van Hateren database Red and black dashed curves in each plot correspond to Gaussian densities of the same mean and variance and the optimally fitted generalized Laplacian densities, respectively.

[1]Though more elaborated filters such as those in [8] can be employed, we found the results are quite independent of the choice of filters.

Laplacian models. However, the statistics of the mean responses are different from the statistics of the raw responses in several important aspects. Especially, our experimental results show that the variance and kurtosis of the mean responses tend to be significantly smaller than those obtained over the raw responses. Such decrease in variance and kurtosis are results of taking average of random variables of finite variances, which tend to reduce the variance, and the resulting density of such averages tends to be more similar to Gaussian (thus with reduced kurtosis) than the original variables. However, the histograms in Fig.1 do not become more alike to Gaussians as would be predicted with the central limit theorem [5], because there are strong statistical dependencies in the derivative domain responses, for which the central limit theorem does not strictly apply [22].

3.3 Maximum Likelihood Estimation of the Vignetting Function

As shown in previous section, we can model the marginal densities of the spatially averaged responses of original natural images in the discrete derivative domains with regards to different derivative types and step sizes with generalized Laplacian densities, as:

$$p_{r,\Delta}(x) \propto \exp\left(-|x/\gamma_{r,\Delta}|^{\beta_{r,\Delta}}\right),$$

with parameters $\beta_{r,\Delta}$ and $\gamma_{r,\Delta}$ estimated from the Van Hateren image database as described in Section 3.2 for each r and Δ. We can reformulate the estimation of vignetting function parameter as to maximize the joint (log) likelihood of $\overline{D^r_\Delta i(\mathbf{v})}$ with regards to different r and Δ. Dropping irrelevant constants, this is equivalent to:

$$\min_\theta \sum_{r,\Delta}\left(\frac{\overline{D^r_\Delta i_v(\mathbf{v})} - \overline{D^r_\Delta \log A(\mathbf{v})} - \overline{D^r_\Delta \log G(\mathbf{v})}}{\gamma_{r,\Delta}}\right)^{\beta_{r,\Delta}}, \quad (6)$$

with a constraint ensuring the shape matrix P to be positive definite, i.e., $p_1 p_3 > p_2^2$. Note that in the above objective function, $\overline{D^r_\Delta i_v(\mathbf{v})}$, $\overline{D^r_\Delta \log A(\mathbf{v})}$ and $\overline{D^r_\Delta \log G(\mathbf{v})}$ are all computed from observed vignetted image and the parametric vignetting function for a given parameter setting θ. The optimization is implemented numerically with coordinate descent. In details, denote the objective function in Eq.(6) as $L(\mathbf{c}, P, \{\alpha_i\}_{i=1}^k)$, the optimization proceeds as alternating between steps that optimizes $\{\alpha_i\}_{i=1}^k$ with $\mathbf{c}$ and P fixed and that optimizes $\mathbf{c}$ and P with $\{\alpha_i\}_{i=1}^k$ fixed. Each of the two optimization steps is efficiently implemented with gradient based numerical methods. The overall coordinate-descent procedure thus guarantees to converge to a local minimum of Eq.(6).

3.4 Gaussian Approximation Initialization

The nonlinear objective function in Eq.(6) have many local minimums, where the choice of the initial parameter values plays a critical role. In this section, we describe a simpler and more efficient method that can be used to find good initial values for the center $\mathbf{c}$ and shape matrix P in the generalized Kang-Weiss model, Eq.(2). This algorithm hinges on two observations. First, the geometric factor $G(\mathbf{v})$ contributes significantly less than $A(\mathbf{v})$ in the vignetting function, and second, the illumination factor $A(\mathbf{v})$can be approximated with a Gaussian function[2]. To see the latter, first note that we have

$$\log A(\mathbf{v}) = \log \frac{1}{\left(1+\left(\frac{r}{2}\right)^2\right)^2} = -2\log\left(1+\left(\frac{r}{2}\right)^2\right).$$

[2]In statistics, this corresponds to the fact that the Gaussian density is a good approximation to the Student's t-density with a large degree of freedom [5].

Next, using the Taylor expansion of log function, $\log(1+x) = x + \mathcal{O}(x^2)$ for $x \geq 0$, we have

$$-2\log\left(1+\left(\frac{r}{2}\right)^2\right) = -\frac{r^2}{2} + \mathcal{O}\left(\left(\frac{r}{2}\right)^4\right).$$

For typical vignetting, the effective focal length is large, and we have $0 < r \ll 1$. We can then drop the higher order terms, exponentiating both sides yields in the above equation to obtain

$$A(\mathbf{v}) \approx \exp(-r^2/2),$$

of which the latter is the Gaussian function for r.

With the Gaussian approximation and dropping the geometric term, Eq.(3) can be simplified into:

$$i_v(\mathbf{v}) = i(\mathbf{v}) - \frac{1}{2}(\mathbf{v}-\mathbf{c})^T P(\mathbf{v}-\mathbf{c}). \quad (7)$$

From Eq.(7), we devise an algorithm to estimate $\mathbf{c}$ and P. For simplicity, we use *continuous* derivative operators to illustrate the general idea first, and then switch to discrete derivative operators to describe the actual implementation.

Taking partial derivatives to both sides of Eq.(7) with regards to x and y, we have

$$\frac{\partial i_v(\mathbf{v})}{\partial x} = \frac{\partial i(\mathbf{v})}{\partial x} - p_1(x-c_1) - p_2(y-c_2), \quad (8)$$

$$\frac{\partial i_v(\mathbf{v})}{\partial y} = \frac{\partial i(\mathbf{v})}{\partial y} - p_3(y-c_2) - p_2(x-c_1). \quad (9)$$

Further taking partial derivatives with regards to x and y to Eq.(8) and (9), we can obtain

$$\frac{\partial^2 i_v(\mathbf{v})}{\partial x^2} = \frac{\partial^2 i(\mathbf{v})}{\partial x^2} - p_1, \quad (10)$$

$$\frac{\partial^2 i_v(\mathbf{v})}{\partial y^2} = \frac{\partial^2 i(\mathbf{v})}{\partial y^2} - p_3, \quad (11)$$

$$\frac{\partial^2 i_v(\mathbf{v})}{\partial x \partial y} = \frac{\partial^2 i(\mathbf{v})}{\partial x \partial y} - p_2. \quad (12)$$

Next, as discussed in Section 3.1, we compute the spatial average over all pixel locations $\mathbf{v}$ to both sides in Eq.(10)-(12), which yields

$$\overline{\frac{\partial^2 i_v(\mathbf{v})}{\partial x^2}} = \overline{\frac{\partial^2 i(\mathbf{v})}{\partial x^2}} - p_1$$

$$\overline{\frac{\partial^2 i_v(\mathbf{v})}{\partial y^2}} = \overline{\frac{\partial^2 i(\mathbf{v})}{\partial y^2}} - p_3$$

$$\overline{\frac{\partial^2 i_v(\mathbf{v})}{\partial x \partial y}} = \overline{\frac{\partial^2 i(\mathbf{v})}{\partial x \partial y}} - p_2$$

As in the general case in Section 3.1, the spatial average gets rid of the dependency to individual pixel locations. These equations show that the elements of the shape matrix are computed as the difference between the spatial averages of second order derivatives of the vignetted image and those of the original image.

Following the general solution given in Section 3.3, we can use the generalized Laplacian models for $\overline{\frac{\partial^2 i(\mathbf{v})}{\partial x^2}}$, $\overline{\frac{\partial^2 i(\mathbf{v})}{\partial y^2}}$ and $\overline{\frac{\partial^2 i(\mathbf{v})}{\partial x \partial y}}$ to find optimal solutions of p_1, p_2 and p_3. On the other hand, as observed empirically (see Fig.1), for natural images with no vignetting effects, the means of the spatial averages of the derivative domain responses tends to be close to zero. This implies an even simpler and more efficient algorithm. Especially, (p_1, p_2, p_3) are directly estimated as

$$p_1 \approx -\overline{\frac{\partial^2 i_v(\mathbf{v})}{\partial x^2}}, \quad p_2 \approx -\overline{\frac{\partial^2 i_v(\mathbf{v})}{\partial x \partial y}}, \quad p_3 \approx -\overline{\frac{\partial^2 i_v(\mathbf{v})}{\partial y^2}}. \quad (13)$$

With P obtained using Eq.(13), we can estimate the center of the vignetting function, $\mathbf{c}$, in a similar fashion. First, we compute the average over all pixel locations $\mathbf{v}$ of the first order partial derivatives given in Eq.(8) and (9). Because we set the origin of the coordinate system for $\mathbf{v} = (x, y)^T$ at the geometric center of the image, which implies that $\sum_x x = 0$ and $\sum_y y = 0$, Eq.(8) and (9) become:

$$\overline{\frac{\partial i_v(\mathbf{v})}{\partial x}} = \overline{\frac{\partial i(\mathbf{v})}{\partial x}} + p_1 c_1 + p_2 c_2, \quad (14)$$

$$\overline{\frac{\partial i_v(\mathbf{v})}{\partial y}} = \overline{\frac{\partial i(\mathbf{v})}{\partial y}} + p_2 c_1 + p_3 c_2. \quad (15)$$

Similarly, assuming the spatial averages of the first order derivatives are close to zero, c_1 and c_2 are then directly obtained by solving the following simple linear equation:

$$\begin{pmatrix} p_1 & p_2 \\ p_2 & p_3 \end{pmatrix} \begin{pmatrix} c_1 \\ c_2 \end{pmatrix} = \begin{pmatrix} \overline{\frac{\partial i_v(\mathbf{v})}{\partial x}} \\ \overline{\frac{\partial i_v(\mathbf{v})}{\partial y}} \end{pmatrix}. \quad (16)$$

3.5 Using Multiple Step Sizes

Eq.(13) and (16) provide simple steps to estimate P and $\mathbf{c}$ using continuous derivative operators. To implement these procedures for discrete pixel lattice, we can simply replace the continuous derivative operators with the corresponding discrete derivative operators. However, if we use the discrete derivative operators corresponding to one step size, the estimation is usually subject to strong statistical fluctuations and becomes much less accurate. Here, we describe a more robust estimation method using discrete derivative operators of multiple step sizes, which are defined in Section 3.1.

We start with the estimation of P. Approximating continuous derivative operators with the corresponding normalized discrete derivative operators of step size Δ in Eq.(13) leads to a quadratic dependence between Δ and $\overline{D^t_\Delta i_v(\mathbf{v})}$ as:

$$\begin{aligned} \overline{D^{xx}_\Delta i_v(\mathbf{v})} &\approx -p_1\Delta^2, \\ \overline{D^{xy}_\Delta i_v(\mathbf{v})} &\approx -p_2\Delta^2, \\ \overline{D^{yy}_\Delta i_v(\mathbf{v})} &\approx -p_3\Delta^2. \end{aligned}$$

In Fig.2, we illustrate such quadratic dependency observed on a synthetic vignetted image, whose vignetting effect are synthetically added using the generalized Kang-Weiss model (see Section 4 for experimental details). The red circles are values for $\overline{D^t_\Delta i_v(\mathbf{v})}$ corresponding to $\Delta = 1, \cdots, 25$, and the black dashed curves correspond to $p_i\Delta^2$ for $i = 1, 2, 3$. Note the strong consistency between the estimated averaged derivative domain responses and the quadratic function of Δ obtained with the true values for (p_1, p_2, p_3).

One approach to combine estimations (p_1, p_2, p_3) based on derivative operators of different step sizes is to use a weighted least squares minimization, whose objective functions are given as:

$$\begin{aligned} p_1^\star &= \underset{p_1}{\operatorname{argmin}} \sum_\Delta w^{xx}_\Delta \left[\overline{D^{xx}_\Delta i_v(\mathbf{v})} + p_1\Delta^2\right]^2, \\ p_2^\star &= \underset{p_2}{\operatorname{argmin}} \sum_\Delta w^{xy}_\Delta \left[\overline{D^{xy}_\Delta i_v(\mathbf{v})} + p_2\Delta^2\right]^2, \\ p_3^\star &= \underset{p_3}{\operatorname{argmin}} \sum_\Delta w^{yy}_\Delta \left[\overline{D^{yy}_\Delta i_v(\mathbf{v})} + p_3\Delta^2\right]^2, \end{aligned}$$

where weights w^{xx}_Δ, w^{xy}_Δ and w^{yy}_Δ are the inverse standard deviations of $\overline{D^{xx}_\Delta i(\mathbf{v})}$, $\overline{D^{xy}_\Delta i(\mathbf{v})}$ and $\overline{D^{yy}_\Delta i(\mathbf{v})}$, respectively, estimated from the set of natural images as described in Section 3.2. These

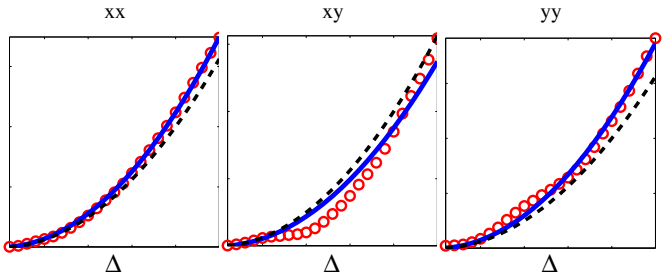

Figure 2: Illustration of the quadratic dependency between Δ and $\overline{D^t_\Delta i_v(\mathbf{v})}$ for $t \in \{xx, xy, yy\}$. Red circles are values for $\overline{D^t_\Delta i_v(\mathbf{v})}$ corresponding to $\Delta = 1, \cdots, 25$ estimated from a synthesized vignetted image of different Δ. Black dashed curves correspond to $p_i\Delta^2$, and blue solid curves correspond to $p_i^\star\Delta^2$, $i = 1, 2, 3$. See text for more details.

weighted least squares estimations afford close-form solutions as:

$$p_1^\star = -\frac{\sum_\Delta w^{xx}_\Delta \overline{D^{xx}_\Delta i_v(\mathbf{v})}\Delta^2}{\sum_\Delta w^{xx}_\Delta \Delta^4}, \quad (17)$$

$$p_2^\star = -\frac{\sum_\Delta w^{xy}_\Delta \overline{D^{xy}_\Delta i_v(\mathbf{v})}\Delta^2}{\sum_\Delta w^{xy}_\Delta \Delta^4}, \quad (18)$$

$$p_3^\star = -\frac{\sum_\Delta w^{yy}_\Delta \overline{D^{yy}_\Delta i_v(\mathbf{v})}\Delta^2}{\sum_\Delta w^{yy}_\Delta \Delta^4}. \quad (19)$$

Once solution of p_1, p_2, p_3 are found, we plug it into Eq.(16), and replace the righthand side with an average over the step size:

$$\begin{pmatrix} p_1^\star & p_2^\star \\ p_2^\star & p_3^\star \end{pmatrix} \begin{pmatrix} c_1 \\ c_2 \end{pmatrix} = \begin{pmatrix} \frac{1}{\Delta}\sum_\Delta \overline{D^x_\Delta i_v(\mathbf{v})} \\ \frac{1}{\Delta}\sum_\Delta \overline{D^y_\Delta i_v(\mathbf{v})} \end{pmatrix}. \quad (20)$$

The center of the vignetting function, $\mathbf{c}$, is then the solution to this simple 2D linear equation.

In summary, Eq.(17)-(19) and (20) provide efficient estimations of the shape matrix and the center of the vignetting function. In practice, we observed that the estimation of P using Eq.(17)-(19) is reasonably accurate, but the estimated $\mathbf{c}$ using Eq.(20) has a higher variance. This may be attributed to that numerically, the weighted least squares estimation for P is more robust, but the matrix inversion in Eq.(20) is less stable.

4. EXPERIMENTS

In this section, we evaluate the performance and running efficiency of our single image vignetting estimation method in reducing vignetting effects and identifying source camera/lens combination.

4.1 Synthetic Vignetted Images

In the first set of experiments, we select 20 RGB JPEG images of 320×480 pixels from the Berkeley image segmentation database [24] that do not have obvious vignetting effects. We apply synthesized vignetting function to these images, and then use the method described in this work to recover the vignetting functions and the original image. As in this case, we have ground truth for both the vignetting functions and the original images, these experiments give us a chance to quantitatively evaluate the performance and running efficiency of the proposed method.

The synthesized vignetting functions are created using the generalized Kang-Weiss model, Eq.(3) with three different settings for the centers and shape matrices as shown in Table 1. Coordinates

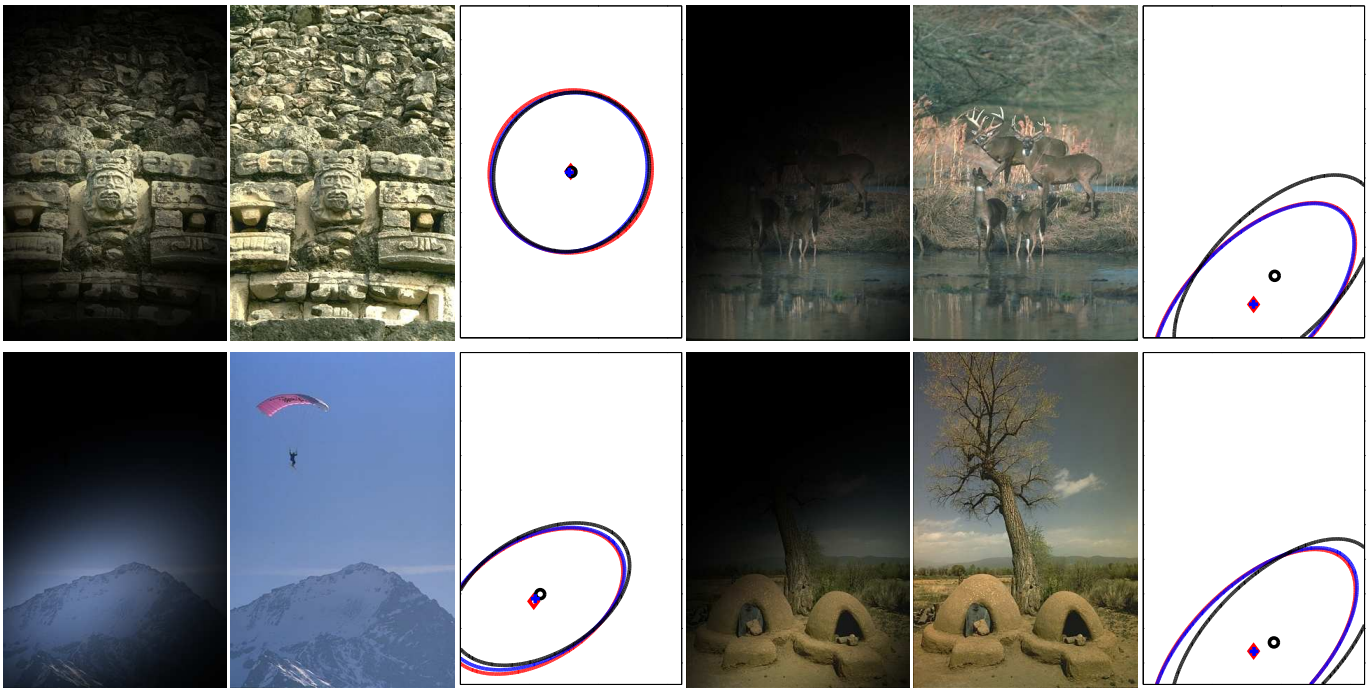

Figure 3: Examples of restoring synthetic vignetted images. Left: vignetted image. Middle: restored image. Right: the estimated centers and shape matrices using their characteristic ellipses. Legend: blue (true vignetting function), black (estimation with Gaussian approximation), red (estimation with maximum likelihood and Gaussian approximation initialization). This figure is better viewed in color.

for the centers are relative to the origin of the coordinate system at the image center. The effective focal length in these cases is 100 pixels, which leads to very strong vignetting for the image sizes used in our experiments as shown in Fig.3. We use the same set of $(\alpha_1, \cdots, \alpha_7)$ for the geometric component $G(\mathbf{v})$, these values are obtained from the estimation of real lens vignetting functions.

	center	shape matrix
setting 1	$\mathbf{c}_1 = \begin{pmatrix} 0 \\ 0 \end{pmatrix}$	$P_1 = \frac{1}{10^4}\begin{pmatrix} 1 & 0 \\ 0 & 1 \end{pmatrix}$
setting 2	$\mathbf{c}_2 = \begin{pmatrix} -80 \\ -60 \end{pmatrix}$	$P_2 = \frac{1}{10^4}\begin{pmatrix} 1 & 0.5 \\ 0.5 & 1.5 \end{pmatrix}$
setting 3	$\mathbf{c}_3 = \begin{pmatrix} 0 \\ -130 \end{pmatrix}$	$P_3 = \frac{1}{10^4}\begin{pmatrix} 1 & 0.6 \\ 0.6 & 1 \end{pmatrix}$

Table 1: Three different settings for the illumination factor part of the generalized Kang-Weiss vignetting model used in our experiments.

We apply these synthetic vignetting functions to the 20 test images, where the same vignetting function is applied to each RGB color channel individually. We then compare the performance of our algorithm with the previous single image vignetting method described in [35][3]. For our method, we use the Gaussian approximation initialization to the nonlinear maximum likelihood optimization as described in the previous section. For the multi-step estimation of the center and shape matrix of the vignetting function in the Gaussian approximation, we use step sizes Δ from 1 to 25. The nonlinear optimization of Eq.(6) is achieved with function `fmincon` in `MATLAB`. The complete MATLAB code reproducing results in this paper can be found at `blindreview`.

We evaluate the quantity of the images with reduced vignetting effects using peak-signal-to-noise ratio (PSNR). The unit of PSNR is deci-bel (dB), for which a higher value suggests better image quality. We use relative errors to measure the quality of the estimated vignetting function parameters. Specifically, for P we use

$$r_P = \frac{\|P^\star - P\|_F}{\|P\|_F},$$

where $\|\cdot\|_F$ is the Frobenius norm. For the estimated center, $\mathbf{c}$, we evaluate accuracy with

$$r_c = \frac{\|\mathbf{c}^\star - \mathbf{c}\|_2}{\|\mathbf{c}\|_2},$$

where $\|\cdot\|_2$ is the l_2 norm. For the parameters in the geometrical factor, $\{\alpha_i\}_{i=1}^k$, we use the following error metric:

$$r_\alpha = \sqrt{\frac{\sum_{i=1}^k (\alpha_i^\star - \alpha_i)^2}{\sum_{i=1}^k \alpha_i^2}}.$$

The running time is based on an unoptimized MATLAB implementation of this algorithm on a machine with due core Intel processor of 2.6GHz and 2GB memory. As the vignetting estimation method in [35] cannot estimate the center and assume diagonal shape matrix (circular image circle), we also include a variant of our method where we make use of the knowledge of the center and the shape matrix (but not the effective focal length). Note that in this case, we do not need the Gaussian approximation for initialization. We report in Table 2 the performance and running efficiency corresponding to the three settings of the synthetic vignetting functions and averaged over all 20 test images.

[3] Runnable code or high-resolution resulting images for [34] or [35] are not publicly available. The reported comparison is based on our own implementation following the description in [35].

Vignetting function setting 1 in Table 1					
	PSNR (dB)	r_P (%)	r_c (%)	r_α (%)	time (sec)
method in [35]	28.7	N/A	N/A	3.5	58.2
known $\mathbf{c}$ and P	28.4	N/A	N/A	4.8	56.4
unknown $\mathbf{c}$ and P	26.8	0.7	4.1	7.4	64.5
Vignetting function setting 2 in Table 1					
	PSNR (dB)	r_P (%)	r_c (%)	r_α (%)	time (sec)
method in [35]	25.8	N/A	N/A	9.2	57.9
known $\mathbf{c}$ and P	28.3	N/A	N/A	3.2	53.3
unknown $\mathbf{c}$ and P	27.4	1.4	5.5	4.6	62.9
Vignetting function setting 3 in Table 1					
	PSNR (dB)	r_P (%)	r_c (%)	r_α (%)	time (sec)
method in [35]	25.9	N/A	N/A	8.3	59.5
known $\mathbf{c}$ and P	28.1	N/A	N/A	2.8	56.4
unknown $\mathbf{c}$ and P	26.7	1.7	6.1	3.4	64.4

Table 2: Performance and running efficiency comparison of different experimental settings. See text for details.

As these results show, when the center and shape matrix of the vignetting function are known, for the first vignetting function in Table 1 where the center coincides with the image center and the shape matrix is diagonal, our method achieves comparable performance and running time as the method in [35]. However, when these conditions do not hold, as for vignetting functions corresponding to setting 2 and setting 3 in Table 1, the estimation obtained with method in [35] becomes much inferior, as the vignetting function does not centered at the image center, and its shape matrix is not circular. On the other hand, our method can estimate the center and shape matrix of the vignetting function along with the geometrical parameters. This advantage comes with only marginal increase in running time in the full algorithm and slight degradation in the quality of the restored image.

In the next set of experiments, we test the effect of Gaussian approximation initialization (Section 3.4) to the overall performance of vignetting estimation. Specifically, we consider the performance under three different program settings:

- **GA only**: using only the Gaussian approximation, Eq.(17)-(19) and (20), to estimate the center and the shape matrix of the vignetting function;
- **ML+rand**: optimizing objective function in Eq.(6) with random initial parameter values;
- **ML+GA**: optimizing object function inEq.(6) with initial shape matrix and center obtained from the Gaussian approximation as in **GA only** case.

We report the performance evaluations and running times corresponding to these three cases and averaged over all three different settings of synthetic vignetting functions in Table 3. Note that the Gaussian approximation is the most efficient (most of the running time actually spent on computing the derivatives with different step sizes), and provides very precise estimation of the shape matrix (GA only). On the other hand, when started with random initial values, the nonlinear optimization is much less effective in terms of both performance and convergence speed (GA + rand). Note also that the estimation of vignetting center is relatively less accurate with the Gaussian approximation initialization, which is compensated by the subsequent nonlinear maximum likelihood estimation.

	PSNR (dB)	r_P (%)	r_c (%)	r_α (%)	time (sec)
GA only	20.7	1.2	24.7	N/A	8.2
ML + rand	25.4	8.9	6.3	7.8	56.4
ML + GA	27.2	0.7	4.1	2.4	64.7

Table 3: Performance and running efficiency evaluation for the Gaussian approximation step in the overall vignetting estimation method.

Fig.3 shows several examples of the restored image from vignetted images with vignetting functions of the three different settings, with the left column corresponding to the vignetted images, the central column corresponding to the restored images, and the right column being the estimated center and shape matrix of the vignetting function. To better visualize the estimated shape matrix, we use its characteristic ellipses corresponding to the ensemble of 2D points $\mathbf{v}$ satisfying $\mathbf{v}^T P \mathbf{v} = 0.5$. As these results show, the Gaussian approximation provides a good estimation of P, but the estimated center $\mathbf{c}$ is much less accurate. On the other hand, together with the nonlinear maximum likelihood optimization, the overall algorithm leads to reasonably accurate estimate of the vignetting function, and vignetting effects are largely removed in the restored images.

4.2 Real Vignetted Images

Next, we test our method on some real vignetted images. In these cases, we do not have the original image, and the estimation is judged by the performance of correcting vignetting effects in these images using the estimated vignetting function. We should point out that the real vignetting functions have less severe attenuation of brightness, compared to the synthetic vignetted images used in the previous set of experiments, with an effective focal length between 500 to 1000 pixels.

Our first set of real vignetted images are selected from the Berkeley database, each with visible vignetting effects. Fig.4 shows the vignetted image (top row) as well as their correction with our method (bottom). For these real vignetted images, the vignetting effects are significantly reduced and the visual appearances are much improved compared to the original vignetted images. However, the restoration results are not perfect, with over-correction for images with complex texture regions (e.g., middle panel of Fig.4). We speculate that such is the result that the parametric vignetting model is only an approximation to the true physical vignetting pattern, and complex scene structures may interfere with the nonlinear optimization.

We also compare the vignetting reduction result using our method with that of using Canon's *Peripheral Illumination Correction* (PIC). PIC is a new functionality provided in the most recent high-end digital cameras manufactured by Canon. The digital processor on the camera chip stores optical characteristics of 26 Canon's most popular stock lenses. Together with the lens parameters, including the aperture, shutter speed, exposure and distance setting at the time of shooting, PIC automatically computes brightness compensation for the captured image in real time. The left image in Fig.5 shows an image with considerable vignetting effects. This image is taken with with a Canon EOS 5D camera with an EF 200mm 1:2.8L II USM lens at an aperture f/8. The image is courtesy of Canon USA Inc. For efficient processing, this image is downsampled by factor 4. And the middle one is the result with the brightness falloff fixed with PIC. On the right is the correction result using the method described in this work. Our method largely remove the vi-

Figure 4: Examples from the Berkeley database with strong vignetting effects (top) and their corrections with our method (bottom).

gnetting effect, and the result is comparable with Canon's built-in vignetting correction function that uses settings of camera/lens including aperture, exposure, shutter speed and focal length at the time of capturing.

4.3 Identifying Source Lens/Camera

As described in Section 3, we test the estimated vignetting function from a single image to identify different source camera/lens combinations. Even though our method can only provide the optimal fitting of the actual vignetting pattern with the generalized Kang-Weiss model, the hope is that the parameters in the estimated models are still sufficiently discriminative to differentiate different camera/lens models.

We now describe our experimental settings. To reflect the variety of cameras and lenses, we use two semi-professional digital SLR cameras, Canon EOS 50D and Nikon D300, and two point-and-shoot cameras, Canon PowerShot SD940 and Nikon CoolPix S640. These cameras are chosen for comparable features (e.g., image sensor sizes and shooting ranges). For the SLR cameras, we combine them with different lenses. Specifically, for Canon EOS 50D, we use two types of lens: Canon EF 28-135mm f/3.5-5.6 IS USM and EF-S 18-200mm f/3.5-5.6 IS. For Nikon D300, we have one lens type, Nikon 18-105mm f/3.5-5.6G ED VR AF-S DX Nikkor Autofocus lens. For simplicity, we will denote hereafter the two Canon lenses as C1 and C2, and the Nikon lens as N1 in the subsequent text.

We take 200 outdoor images using each of these camera/lens combinations. For the SLR cameras, with each type of lenses, the images are taken with maximum focal length, and with two different aperture settings, f/4 and f/8. The images are taken with the cameras automatically choosing shutter speed (aperture priority mode). The vignetting compensation mechanism, if applicable, is turned off, so we can analyze the effect of our algorithm. The two point-and-shoot cameras have built-in lenses, and we are not able to directly control the aperture or the focal length. In these cases, we try to focus the camera to an object as far away as possible, and let the cameras to choose automatically for the aperture, exposure and shutter speed. All images are in lossless JPEG format. To simplify the computation, we convert all color images into grayscale using standard luminance transform. This experimental setting results in a total of 1600 images.

We then run the described vignetting estimation method to each of these 1600 images. From each of the estimated vignetting functions, we construct a 10 dimensional feature vector consisting of $(p_1, p_2, p_3, \alpha_1, \cdots, \alpha_7)$, i.e., the components in the shape matrix and the parameters of the geometric factors in the Kang-Weiss vignetting model. We then separate the 1600 feature vectors into two sets, each with 800 feature vectors corresponding to an equal segmentation of images of each specific camera/lens combination. We use one set of 800 vignetting feature vectors as training data to construct a nearest neighbor classifier, and test the obtained classifier on the remaining 800 feature vectors. The top table in Fig.6 shows the confusing matrix on the classification of the testing 800 feature vectors. It suggests that these features are adequate for differentiating the source camera/lens combinations of the test images, with the best performance achieved with the SLR cameras. On the other hand, the performance on the point-and-shoot cameras are limited due to the lack of control over the lens parameters, especially the changes in the effective focal lengths. Note also that these features are particular effective distinguishing lenses of different manufactures (in this case, Canon and Nikon), as relatively smaller classification errors exist for different models.

We also investigate the relative effects of the two types of features in the feature vector, especially, the classification performance with only parameters from the geometrical factors. Shown in the bottom of Fig.6 is the confusion matrix for the same testing set, but the nearest neighbor classifier is constructed with only the 7 parameters in the geometrical components, i.e., $(\alpha_1, \cdots, \alpha_7)$. As the effective focal length (the shape matrix) is discounted, classification errors among same camera/lens combination but with different apertures become worse. On the other hand, classification errors on the point-and-shoot cameras seem to be effectively improved. These are all due to the fact that the reduced feature set uses only geometrical characteristics of the lenses to distinguish different camera/lens combinations.

5. CONCLUSION

In this work, we have presented a new single image vignetting es-

Figure 5: Vignetting correction results for images with physical vignetting. Left: a vignetted image captured with a Canon EOS 50D camera. (Courtesy of Canon USA, Inc.) Middle: image with vignetting corrected using Canon's *Peripheral Illumination Correction* tool. Right: vignetting corrected with our method.

	Canon C1 f/4	Canon C1 f/8	Canon C2 f/4	Canon C2 f/8	Canon PS	Nikon N1 f/4	Nikon N1 f/8	Nikon CP
Canon C1 f/4	61	17	12	1	4	3	1	1
Canon C1 f/8	19	55	6	9	11	0	0	0
Canon C2 f/4	12	7	58	10	12	1	0	0
Canon C2 f/8	7	14	11	63	4	0	1	0
Canon PS	2	13	12	9	43	7	6	5
Nikon N1 f/4	0	0	1	0	1	59	24	15
Nikon N1 f/8	0	1	0	3	1	13	70	12
Nikon CP	1	1	1	0	12	21	18	46

	Canon C1 f/4	Canon C1 f/8	Canon C2 f/4	Canon C2 f/8	Canon PS	Nikon N1 f/4	Nikon N1 f/8	Nikon CP
Canon C1 f/4	43	38	4	3	7	2	1	2
Canon C1 f/8	32	37	12	9	9	0	1	0
Canon C2 f/4	11	7	39	33	5	1	2	2
Canon C2 f/8	8	10	28	42	11	0	0	1
Canon PS	5	7	8	9	67	2	1	1
Nikon N1 f/4	2	1	2	2	3	45	36	9
Nikon N1 f/8	3	13	4	2	3	29	42	4
Nikon CP	0	0	1	3	2	9	11	74

Figure 6: Confusion matrices (in percentage) for the classification of the 8 camera/lens combinations using nearest neighbor classifier and features from the estimated vignetting functions using our method. (Top) Confusion matrix using the full 10 dimensional feature vector. (Bottom) Confusion matrix using only 7 parameters from the geometric components of the Kang-Weiss model. See text for more details.

timation method, and show its effectiveness to identify camera/lens combination of an image. Our method is based on a parametric model of the vignetting function and regular statistical properties of natural images. We start by log transforming the vignetted image and then working in the discrete derivative domains. Based on properties of the mean discrete derivative responses of natural images with no vignetting effect, we reformulate vignetting correction as maximum likelihood estimation of the vignetting function parameters. We further describe a simple and efficient method that uses a Gaussian approximation to the vignetting function to provide good initial values for the nonlinear maximum likelihood estimation. Compared to previous single image vignetting correction methods [34, 35], our method does not require image segmentation or the vignetting function to be centered at the image center, and it also works when the vignetting function has an elliptical shape. Empirical evaluations of the proposed method using synthesized and real vignetted images show significant gain in both performance and running efficiency. Further, in digital image forensics, optical characteristics of a lens can be used for its identification. As the vignetting function are specific for different lenses, our preliminary evaluations show that the estimated vignetting functions can be used to identify stock lenses.

There are several directions we would like to further pursue based on our current work. First, we are currently working on to further quantify the performance of the vignetting function features in identifying camera/lenss using a much larger and comprehensive databases, and including more different camera/lens models. Also, we are interested in combining the features described in this work with other lens (e.g., chromatic aberrations [16]) and camera features (e.g., [6, 12, 18]) for more reliable authentication of digital images.

Acknowledgement

This work was supported by an NSF CAREER Award (IIS09-53373) and the University at Albany Faculty Research Awards Program (FRAP) - Category A. The author would like to thank Hany Farid for pointing out this problem and inspiring discussions.

6. REFERENCES

[1] A.Levin and Y.Weiss. User assisted separation of reflections from a single image using a sparsity prior. In *ECCV*, 2004.

[2] N. Asada, A. Amano, and M. Baba. Photometric calibration of zoom lens systems. In *ICPR*, 1996.

[3] R. Baddeley. Searching for filters with "interesting" output

distributions: an uninteresting direction to explore. *Network*, 7:409–421, 1996.

[4] P.J. Burt and E.H. Adelson. The Laplacian pyramid as a compact image code. *IEEE Transactions on Communication*, 31(4):532–540, 1981.

[5] G. Casella and R. L. Berger. *Statistical Inference*. Duxbury Press, 2nd edition, 2001.

[6] M. Chen, J. Fridrich, M. Goljan, and J. Lukas. Determining image origin and integrity using sensor noise. *IEEE Transactions on Information Forensics and Security*, 3(1):74–90, March 2008.

[7] H. Farid. Photo fakery and forensics. In *Advances in Computers*. 2009. (to appear).

[8] H. Farid and E.P. Simoncelli. Differentiation of discrete multi-dimensional signals. *IEEE Trans. Image Proc.*, 13(4):496–508, 2004.

[9] R. Fergus, B. Singh, A. Hertzmann, S. T. Roweis, and W. T. Freeman. Removing camera shake from a single photograph. In *ACM SIGGRAPH*, 2006.

[10] Thomas Gloe, Karsten Borowka, and Antje Winkler. Feature-based camera model identification works in practice results of a comprehensive evaluation study. In S. Katzenbeisser and A.-R. Sadeghi, editors, *IH 2009, LNCS 5806,*, pages 262–276, 2009.

[11] D. B. Goldman and J. H. Chen. Vignette and exposure calibration and compensation. In *ICCV*, 2005.

[12] Y-F. Hsu and S-F. Chang. Image splicing detection using camera response function consistency and automatic segmentation. In *International Conference on Multimedia and Expo*, Beijing, China, 2007.

[13] J. Huang and D. Mumford. Statistics of natural images and models. In *CVPR*, 1999.

[14] A. Hyvärinen, J. Hurri, and P. O. Hoyer. *Natural Image Statistics: A probabilistic approach to early computational vision*. Springer, 2009.

[15] J. Jia and C.-K. Tang. Tensor voting for image correction by global and local intensity alignment. *IEEE Trans. PAMI*, 27(1):36–50, 2005.

[16] M.K. Johnson and H. Farid. Exposing digital forgeries through chromatic aberration. In *ACM Multimedia and Security Workshop*, Geneva, Switzerland, 2006.

[17] S. Kang and R. Weiss. Can we calibrate a camera using an image of a flat textureless lambertian surface? In *ECCV*, 2000.

[18] M. Kharrazi, H.T. Sencar, and N Memon. Blind source camera identification. In *Proceedings of the 2004 IEEE International Conference on Image Processing (ICIP 2004),*, pages 709–712, 2004.

[19] Rudolf Kingslake and R. Barry Johnson. *Lens Design Fundamentals*. Academic Press, 2nd edition, 2009.

[20] A. Levin, A. Zomet, and Y. Weiss. Learning how to inpaint from global image statistics. In *ICCV*, 2003.

[21] A. Litvinov and Y. Y. Schechner. Addressing radiometric nonidealities: A unified framework. In *CVPR*, 2005.

[22] S. Lyu and E. P. Simoncelli. Reducing statistical dependencies in natural signals using radial Gaussianization. In *NIPS*, 2008.

[23] S G Mallat. A theory for multiresolution signal decomposition: The wavelet representation. 11:674–693, 1989.

[24] D. Martin, C. Fowlkes, D. Tal, and J. Malik. A database of human segmented natural images and its application to evaluating segmentation algorithms and measuring ecological statistics. In *ICCV*, 2001.

[25] A.C. Popescu and H. Farid. Exposing digital forgeries in color filter array interpolated images. *IEEE Transactions on Signal Processing*, 53(10):3948–3959, 2005.

[26] Sidney F. Ray. *Applied photographic optics*. Focal Press, 3rd edition, 2002.

[27] S. Roth and M. Black. Fields of experts: A framework for learning image priors. In *CVPR*, 2005.

[28] D. Ruderman. The statistics of natural images. *Network : Comp. in Neural Sys.*, 5:598–605, 1994.

[29] A. A. Sawchuk. Real-time correction of intensity nonlinearities in imaging systems. *IEEE Trans. Computers*, 26(1):34–39, 1977.

[30] E P Simoncelli and E H Adelson. Noise removal via Bayesian wavelet coring. In *ICIP*, 1996.

[31] A. Swaminathan, Min Wu, and K.J.R. Liu. Digital image forensics via intrinsic fingerprints. *IEEE Transactions on Information Forensics and Security*, 3(1):101–117, March 2008.

[32] A van der Schaaf and J H van Hateren. Modelling the power spectra of natural images: Statistics and information. *Vision Research*, 28(17):2759–2770, 1996.

[33] W. Yu. Practical anti-vignetting methods for digital cameras. *IEEE Trans. on Cons. Elect*, 50(2):975–983, 2004.

[34] Yuanjie Zheng, Stephen Lin, and Sing Bing Kang. Single-image vignetting correction. In *CVPR*, 2006.

[35] Yuanjie Zheng, Jingyi Yu, Stephen Lin, Sing Bing Kang, and Chandra Kambhamettu. Single-image vignetting correction using radial gradient symmetry. In *CVPR*, 2008.